Author Manuscript

Author Manuscript

Author Manuscript

Author Manuscript

HHS Public Access

Author manuscript

Int J Numer Method Biomed Eng. Author manuscript; available in PMC 2019 February 18.

Published in final edited form as:

Int J Numer Method Biomed Eng. 2018 September ; 34(9): e3111. doi:10.1002/cnm.3111.

Modeling hemodynamics in intracranial aneurysms: Comparing accuracy of CFD solvers based on finite element and finite volume schemes

Lorenzo Botti[†], **Nikhil Paliwal**[◇,*], **Pierangelo Conti**[†], **Luca Antiga**[‡], and **Hui Meng**[★,◇,*,♣]

[★]Department of Mechanical and Aerospace Engineering, University of Buffalo

[◇]Toshiba Stroke and Vascular Research Center, University of Buffalo

[*]Department of Neurosurgery, University at Buffalo

[♣]Department of Biomedical Engineering, University at Buffalo

[†]Department of Engineering and Applied Science, University of Bergamo

[‡]Orobix SRL, Bergamo

Abstract

Image-based computational fluid dynamics (CFD) has shown potential to aid in the clinical management of intracranial aneurysms (IAs) but its adoption in the clinical practice has been missing, partially due to lack of accuracy assessment and sensitivity analysis. To numerically solve the flow-governing equations CFD solvers generally rely on two spatial discretization schemes: Finite Volume (FV) and Finite Element (FE). Since increasingly accurate numerical solutions are obtained by different means, accuracies and computational costs of FV and FE formulations cannot be compared directly. To this end, in this study we benchmark two representative CFD solvers in simulating flow in a patient-specific IA model: (1) ANSYS Fluent, a commercial FV-based solver and (2) VMTKLab multidGetto, a discontinuous Galerkin (dG) FE-based solver. The FV solver's accuracy is improved by increasing the spatial mesh resolution (134k, 1.1m, 8.6m and 68.5m tetrahedral element meshes). The dGFE solver accuracy is increased by increasing the degree of polynomials (first, second, third and fourth degree) on the base 134k tetrahedral element mesh. Solutions from best FV and dGFE approximations are used as baseline for error quantification. On average, velocity errors for second-best approximations are approximately 1cm/s for a [0,125]cm/s velocity magnitude field. Results show that high-order dGFE provide better accuracy per degree of freedom but worse accuracy per Jacobian non-zero entry as compared to FV. Cross-comparison of velocity errors demonstrates asymptotic convergence of both solvers to the same numerical solution. Nevertheless, the discrepancy between under-resolved velocity fields suggests that mesh independence is reached following different paths.

1 Introduction

Image-based Computational Fluid Dynamics (CFD) has been increasingly employed to investigate the role of hemodynamics in initiation, growth and rupture of intracranial aneurysms (IAs) see *e.g.* [16]-[18]-[26]-[27]. Multiple studies have shown the association of IA rupture risk with hemodynamic parameters like wall shear stress and oscillatory shear

Author Manuscript Author Manuscript Author Manuscript Author Manuscript

index [17]-[36]-[18], which could potentially aid the clinicians in the management of IAs. However, for CFD to transition from research to aid in clinical management of IAs, it is important to quantify and compare the accuracy of candidate CFD solvers, sharpening the influence of solver parameters on the reliability of the simulated hemodynamic results [29]. In fact, the whole simulation workflow, from segmentation of medical images to mesh generation and, finally, computational simulations to obtain hemodynamics needs to be investigated. However, this study focuses on the CFD solver employed in this whole simulation workflow. In particular we ought to investigate the computational cost required to reach mesh independence since the computational expense can be significant and can differ for different approximation schemes.

CFD solvers based on Finite Element (FE) and Finite Volume (FV) methods are among the most celebrated in the biomedical community owing to their handling of complex anatomical geometries. While part of the IA research community has developed open-source FE-based solvers [14]-[10]-[34], most of the researchers prefer commercially available FV-based CFD solvers which are robust, validated, user-friendly and supplemented by reliable mesh generators [9]-[23]. Although both CFD approaches numerically solve the flow-governing Incompressible Navier-Stokes (INS) equations in order to simulate hemodynamics in IAs, there is an intrinsic difference in FE and FV spatial discretizations leading to different approximation properties. Form the temporal discretization viepoint both FE and FV CFD solvers rely on ad-hoc time integration strategies. Decoupled schemes based on the Pressure Poisson Equation (PPE) or block preconditioners for Differential Algebraic Equations (DAEs) systems are usually employed for the sake of efficiency, see *e.g.* Temam [32] and Benzi *e.a.* [8], respectively. Recently, alongside ubiquitous FV-based CFD formulations, discontinuous Galerkin FE methods (dGFEM) are gaining momentum for their efficacy and reliability in handling complex CFD applications. Several research efforts have proposed and investigated efficient solution strategies for dGFEM discretizations of incompressible flow problems, see *e.g.* [31]-[13]-[25]-[12].

Both FV and FE schemes achieve high-order of accuracy increasing the mesh density (or *h*-refinement), but, in order to exploit the favourable convergece properties of higher-order discretizations, the degree of dGFE polynomial spaces can be increased keeping the mesh fixed (or *p*-refinement). The aim of the present study is to provide an objective comparison of increasingly accurate FV and dGFE hemodynamic computations performed in a complex patient-specific IA geometry. Instead of validating against experiments, asymptotic convergence is assessed cross-comparing *h*-refined FV with *p*-refined dGFE computations. The primary goal is to identify the mesh density and the polynomial degree required to approach mesh independence in steady state simulations. The secondary goal is to objectively compare FV and dGFEM solvers based on the number of degrees of freedom and sparsity of the Jacobian matrix (the number of non-zeroes entries of the Jacobian matrix will be considered). We do not pretend to identify the best numerical strategy but rather to estimate accuracy and computational expense objectively. In particular we neglect wall clock time comparison due to the influence of efficacy, fine-tuning and scalability of the solution strategy.

Author Manuscript Author Manuscript Author Manuscript Author Manuscript

The material in this paper is organized as follows. In Section 2.2 we introduce the computational flow domain and its discretization by means of a *h*-refined mesh sequence. The prescribed flow conditions are described in Section 2.3. Section 3 tackles the computational methods. As a first point we briefly review FVM and dGFEM focusing on asymptotic convergence rates of increasingly accurate spatial discretizations, thus we give some details regarding the solution strategy, the iterative solver parameters and the convergence history. The comparison of increasingly accurate FV and dG solutions based on achieved precision and computational expense is presented in Section 4. Our comparison metrics provides a fair ground for cross-evaluating the influence of mesh density and polynomial degree on computational hemodynamics in the IA model. We hope that this work will contribute to raise the awareness of the subtleties involved in using CFD and will provide additional tools to critically evaluate computational studies.

2 Hemodynamics of a patient specific intracranial aneurysm geometry

2.1 Spatial discretizations comparison based on increasingly accurate hemodynamics

Comparison of hemodynamic computations in vascular models based on *h*-refined FV discretizations and *p*-refined dG discretizations is challenging because of the lack of an analytical description of the complex vascular geometry. On one hand *h*-refined mesh sequences intrinsically improve the approximation of the computational domain boundaries allowing them to closely replicate the vessel wall smoothness. On the other hand *p*-refinement implies that the grid cardinality is fixed and improvements of the computational geometry must be pursued by means of higher-order curved elements meshes [33]. Since different domain boundaries approximations prevent numerical schemes from reaching same numerical solutions, in this study we fix the domain boundaries representation for the FV and FE schemes. This allows us to safely compare different scheme's convergence strategies without introducing a bias related to the mesh generation technique. Indeed, even if the accuracy of the numerical solution with respect to the (unknown) exact solution on the (unknown) exact geometry might be impacted by a rougher computational geometry, the convergence properties with respect to the exact solution on the approximated geometry are not altered. Accordingly, the accuracy obtained on the approximated geometry is representative of the accuracy that would be obtained considering more precise approximations of the domain geometry.

2.2 The computational domain and its discretization

The computational domain Ω_H is a patient-specific IA geometry reconstructed from medical images. After approval by University of Buffalo institutional review board, 3D-Digital Subtraction Angiography (DSA) is employed for aneurysm evaluation. The Internal Carotid Artery (ICA) aneurysm is located sidewall, immediately after a double bend of the carotid syphon. The aneurysm sac and inlet radius measures 9mm and 1.3mm, respectively. For image segmentation and surface mesh generation we relied upon the open-source Vascular Modelling Toolkit (VMTK) [1]. Vessel walls are approximated by means of a 28k triangular elements mesh. Starting from the computational domain boundaries $\partial\Omega_H$, the reference volume mesh $\mathscr{T}_1$ approximating Ω_H is generated by means of the open source software Gmsh [21], see Figure 1. The element size is kept proportional to the curvature of vessel

Author Manuscript Author Manuscript Author Manuscript Author Manuscript

walls for a total of 134k tetrahedral elements. The average, maximum and minimum element measures are 5.52×10^{-3}, 5.73×10^{-2} and 2.37×10^{-4} mm^3, respectively. Next, in order to obtain a sequence of four h-refined grids $\{\mathcal{T}_i\}_{i=1,2,3,4,}$ $\mathcal{T}_1$ is uniformly refined four times. At each refinement step each tetrahedral element is subdivided in 8 tetrahedral sub-elements, such that card $(\mathcal{T}_i) = 8^{i-1}$ card $(\mathcal{T}_1)$, where card $(\mathcal{T}_i)$ represents the cardinality of the mesh set $(\mathcal{T}_i)$. Accordingly the mesh step size h halves at each refinement step, that is $h_i = \frac{h_1}{2^{i-1}}$. The finer mesh tops at 68.5m tetrahedral elements. Clearly, defining $\partial\mathcal{T}_i$ as the union of the boundary faces of the volume mesh, we have $\partial\mathcal{T}_i = \partial\Omega_H$.. This trivial refinement strategy does not cluster elements near the vessel walls to better capture boundary layers but maintains a uniform mesh quality and allows to obtain a sequence of nested grids (where each element of $\mathcal{T}_i$, $i = 2, 3, 4$, is contained in exactly one element of $\mathcal{T}_{i-1}$).

2.3 Prescribed flow conditions

Since the focus is on the accuracy of FV and dGFEM spatial discretizations we consider steady state flow conditions for this study. This is a preliminary step prior to tackling unsteady pulsatile flow conditions, where the accuracy of the temporal discretization also comes into play. In fact, in order to correctly estimate the temporal error, the spatial discretization error must be small enough.

The flow domain has one inlet and one outlet where a plug-flow and a traction-free boundary conditions are imposed, respectively. The plug-flow instead of a fully developed Poiseuille velocity profile was chosen for simplicity. The computational domain is extended in the outward normal direction with respect to the inflow artificial boundary (with the so called *flow extension*) in order to ensure that the flow is fully developed prior to the first bend. At the vessel walls a no-slip boundary conditions is imposed.

We consider a physiological flow rate of 260 ml/ min corresponding to an inflow Reynolds number of approximately 600. The Reynolds number is high enough that convection balances/dominates diffusion, as confirmed by the complexity of velocity profiles observed over transversal sections all along the vessel centerline. The tortuosity of the carotid syphon produces a non-trivial flow behavior: the bulk of the flow tends to occupy the outward portion of the bend while recirculating secondary vortices develop within the cornering arc downstream to the bend.

3 Computational methods

This section provides details about the solution strategies and setups of the two CFD solvers compared in this work. multidGetto (VMTKLab's solver) relies on a dG discretization while Fluent (ANSYS Inc., Canonsburg, PA) on a FV discretization. Interestingly, dGFEM and FVM share some common features: i) They are well suited to discretize conservation laws written in flux divergence conservative form, where the unknown variables appear as argument of flux functions. ii) They rely on a discrete form of the control volume method where each cell of the discretized flow domain is treated as an individual control volume. iii)

Author Manuscript Author Manuscript Author Manuscript Author Manuscript

The definition of suitable numerical fluxes at inter-element boundaries (the surfaces bounding each cell's control volume) ensure conservation of physical quantities and the coupling between neighboring elements.

However, the main differences between these solution schemes hinge on the solution representation.

- FV: in each mesh element, each unknown variable's degree of freedom (DOF) is its cell averaged value.
- dG: in each mesh element, each unknown variable's degrees of freedom (DOFs) are the coefficients of its polynomial expansion of degree $k \geqslant 1$.

Accordingly, if fluxes are functions of both the variables and the gradient of variables, also the way spatial derivatives are computed differs.

- FV: the gradient is *reconstructed* using averaged values of neighboring cells.
- dG: the gradient is evaluated in an element-by-element fashion computing the spatial derivatives of the polynomial expansion.

Both methods rely on conservation laws in flux divergence conservative form integrated over each mesh element. The following procedure is applied to obtain the spatial discretizations.

- FV: cell integrals involving the divergence of flux functions are rewritten as surface integrals of (numerical) fluxes using the divergence theorem.
- dG: cell integrals are multiplied by a suitable *test* function and the terms involving the divergence of flux functions are integrated by parts.

Definition of numerical fluxes completes the definition of the method in case of FV. dGFEM also requires to introduce piecewise polynomial spaces whose the solution as well as the test function belongs to, and quadrature rules for numerical integration over mesh elements and mesh faces.

In this work we solve the steady constant density INS equations for Newtonian fluids. The continuity equation coupled with the momentum equation for the conservation of mass and momentum are discretized by means of dGFEM and FV discretizations.

3.1 Discontinuous Galerkin Finite Element Method

We apply the fully coupled spatial dG discretization introduced by Bassi *e.a.* [4] which relies on the artificial compressibility approach devised by Chorin [19] to recover the hyperbolicity at inter-element boundaries. In particular, based on the Godunov's scheme approach, the convective numerical flux is computed by solving Riemann problems associated to the artificial compressibility perturbation of the one dimensional Euler equations, see Elsworth and Toro [20] and Bassi *e.a.* [5] for more details. Since artificial compressibility is introduced only at the interface flux level, the resulting INS equations discretization is consistent irrespective of the amount of artificial compressibility introduced. The artificial compressibility flux allows for equal polynomial degree velocity-pressure formulations and

Author Manuscript Author Manuscript Author Manuscript Author Manuscript

improves solver's robustness when dealing with convection dominated flows. The viscous term is discretized by means of the BR2 formulation, see [6].

Unknown *trial* functions (representing the unknown variables) and *test* functions belong to the following polynomial space

$$\mathscr{P}_k(\mathscr{T}_h) := \left(\bigtimes_{T \in \mathscr{T}_h} \mathbb{P}_k(T) \right) \quad (1)$$

where $\mathbb{P}_k(T)$ is the space of polynomial functions in three variables (one for each space dimension) and total degree $\leqslant k$ defined over each mesh element T. Accuracy of dG discretizations can be improved refining the grid (h-refinement) or increasing the polynomial degree of discrete spaces (p-refinement). If the same polynomial degree is employed for each velocity component and for pressure, the resulting dG discretization converges as h^{k+1} and h^k for the velocity and pressure error in $L^2(\Omega_H)$ norm, respectively. The polynomial degree can be chosen to be arbitrarily high, and consisting of arbitrarily shaped elements. Fast exponential convergence is obtained in p-refinement (increasing k and keeping the grid fixed), faster than any power of h. The steady state solution is sought by means of the Pseudo-Transient-Continuation method by Kelley and Keyes [24], a globalization strategy that improves convergence of Newton's method in the presence of rough initial guesses. Jacobian matrices are exactly computed leading to a fully implicit fully coupled strategy. The Successive Evolution Relaxation (SER) strategy by Mulder *e.a.* [28] is employed for evolving the pseudo time step and the adaptive forcing term choice proposed by Botti [11] is applied to avoid *oversolving* of the Newton equations. The agglomeration based h-multigrid solver strategies proposed by Botti *e.a.* [12] is employed to efficiently solve the linearized equations systems of Newton's method.

3.1.1 Increasing the accuracy of steady state dGFEM hemodynamics—

In this work we approximate hemodynamics in the IA geometry by means of p-refined dG discretizations on the coarse grid $\mathscr{T}_1$. Since p-convergence is steeper than h-convergence, see *e.g.* [2], we do not consider h-refined dG discretizations. We employ polynomial spaces of degree $k = 1, 2, 3, 4$, corresponding to linear, quadratic, cubic and quartic polynomials in each mesh element $T \in \mathscr{T}_1$. All computations are initialized with fluid at rest and steady state is reached when the Euclidean norm of residual vector, or alternatively the Euclidean norm of the solution increment vector, drops below 10^{-12}. Simulations are run on the Cineca's Marconi HPC facility (x86 Intel Xeon architecture, two 18 cores CPUs per node). $k = 1, 2, 3, 4$ dG solutions are computed in parallel using 8,36,72 and 144 MPI processes, respectively. The $k = 4$ steady state solution is reached in 53 pseudo-transient continuation steps, for a total of 213 h-multigrid V-cicle preconditioned FGMRES (Flexible GMRES) iterations. Iteration count is almost independent from the polynomial degree, as already reported in [12]. V-cycle relies on two coarse agglomerated elements meshes in addition to the fine grid, for a total of three multigrid levels. At each agglomeration step a seven-fold decrease of the grid cardinality is observed. At each level but the coarsest a single iteration of GMRES is employed as a smoother. GMRES is preconditioned with an Additive

Author Manuscript Author Manuscript Author Manuscript Author Manuscript

Schwartz domain decomposition Method (ASM) which relies on a Incomplete Lower Upper (ILU) decomposition in each sub-domain. At the coarsest level the convergence criterion for the GMRES iteration is set such that the relative residual norm drops below 10^{-4}.

3.2 Finite Volume Method

As a representative FV CFD solver, we employed the commercially popular ANSYS Fluent to solve the steady INS equations, hereinafter be referred to as the FV solver. We set accuracy to second order for the momentum (second order upwind) and the continuity equation, and rely on the recently introduced fully-coupled pressure-based solver. The gradient is reconstructed using the cell-based least square approach.

3.2.1 Increasing the accuracy of steady state FVM hemodynamics—The solution is computed on the sequence of uniformly h-refined grids $\{\mathcal{T}_i\}_{i=1,2,3,4}$, see Section 2.2, where both the velocity and the pressure error in $L^2(\Omega_H)$ norm are expected to converge as h^2. FV computations are performed in parallel using 4,8,12 and 28 processes for $i = 1, 2, 3, 4$, respectively, on a proprietary HPC resource at the University of Bergamo. Convergence to steady state is achieved when the residual of the continuity and momentum equation stagnates around a constant value. Residual of the momentum equation drops below 10^{-12} in 550 and 700 multigrid iteration for computations on $\mathcal{T}_3$ and $\mathcal{T}_4$ respectively. Stagnation around 10^{-7} and 10^{-9} is observed after 200 and 300 multigrid iterations for computations on $\mathcal{T}_1$ and $\mathcal{T}_2$ respectively. Upon convergence to steady state, residual of the continuity equation is two orders of magnitude higher than the residual of momentum. As already stated in the introduction, no attempt has been made to optimize Fluent solver's parameters. Default options are employed.

4 Comparison of FV and dGFEM

After having computed four increasingly accurate FV and dGFEM numerical solutions by means of uniform h-refinement and uniform p-refinement, respectively, the most accurate solutions for both schemes are considered as a reference to evaluate the error of less resolved approximations. In order to provide a metric for comparing the accuracy also the number of DOFs and Jacobian matrix Non-Zeroes entries (JNZs) is evaluated.

4.1 Degrees of freedom and Jacobian matrix sparsity

The total number of DOFs reads

$$\text{dG DOFs} = N_{\text{vars}} \dim\left(\mathcal{P}_k\left(\mathcal{T}_i\right)\right), \quad (2)$$

$$\text{FV DOFs} = N_{\text{vars}} \operatorname{card}\left(\mathcal{T}_i\right), \quad (3)$$

Author Manuscript Author Manuscript Author Manuscript Author Manuscript

where $N_{\text{vars}} = 4$ for the INS equations in three space dimensions (three velocity components plus pressure), and

$$\dim\left(\mathscr{P}_k\left(\mathscr{T}_h\right)\right) = \text{card}\left(\mathscr{T}_i\right)\dim\left(\mathbb{P}_k\right), \quad (4)$$

$$\dim\left(\mathbb{P}_k\right) = \frac{(k+1)(k+2)(k+3)}{6}, \quad (5)$$

see definition 1. Note that the number of DOFs associated to each mesh element $T \in \mathscr{T}_i$ reads

$$\text{dG DOFs}(T) = N_{\text{vars}}\dim\left(\mathbb{P}_k\right), \quad (6)$$

$$\text{FV DOFs}(T) = N_{\text{vars}}. \quad (7)$$

The Jacobian is a sparse square matrix of order equal to the number of DOFs. The matrix has a block structure where diagonal and off-diagonal blocks represent element and inter-element contributions of the spatial discretization, respectively. The number of off-diagonal blocks is equal to the number of neighbors of each mesh element. The order of each square block is $(\text{DOFs}(T))^2$. Accordingly, the total number of Jacobian Non-Zeroes entries (JNZs) can be estimated as follows

$$\text{dG}: \text{JNZs} \simeq \text{card}\left(\mathscr{T}_i\right)\left(\overline{N}_{\text{elem Neighbors}}+1\right)\left(N_{\text{vars}}\dim\left(\mathbb{P}_k\right)\right)^2 \quad (8)$$

$$\text{FV}: \text{JNZs} \simeq \text{card}\left(\mathscr{T}_i\right)\left(\overline{N}_{\text{elem Neighbors}}+1\right)\left(N_{\text{vars}}\right)^2 \quad (9)$$

where the average number of element neighbors is $\overline{N}_{\text{elem Neighbors}} \simeq 4$ for a tetrahedral element mesh. Note that $N_{\text{elemNeighbors}} < N_{\text{faces}} = 4$ for each tetrahedral element adjacent to the computational domain boundary $\partial\Omega_H$.

The number of DOFs and JNZs for increasingly accurate dG and FV computations is reported in Table 1. dGFEM's DOFs and JNZs increase at a lower pace with respect to FVM's eight fold increase. While dG $\mathscr{P}_1\left(\mathscr{T}_1\right)$ has four times more DOFs than FV on $\mathscr{T}_1$, dG $\mathscr{P}_4\left(\mathscr{T}_1\right)$ has approximately fifteen times less DOFs than FV on $\mathscr{T}_4$. Similarly the JNZs ratio drops to two and a half starting from sixteen.

Author Manuscript Author Manuscript Author Manuscript Author Manuscript

4.2 Accuracy evaluation

Let's introduce the set C collecting the centroids of all mesh elements $T \in \mathcal{T}_4$, so that card $(\mathscr{C}) = 68.5m$ and $C \in \mathscr{C}$ is the centroid of mesh element T. The relative velocity errors in L^1-norm are computed as follows

$$E^{\mathrm{dG}_k,\mathrm{FV}_4}_{L^1(\Omega_H)} := \frac{\sum_{C\in C}\left\|\mathrm{v}^{\mathrm{dG}}_{\mathscr{P}k,h_1}(C)-\mathrm{v}^{\mathrm{FV}}_{h_4}(C)\right\|}{\mathrm{card}(\mathscr{C})} \quad (10)$$

$$E^{\mathrm{FV}_i,\mathrm{dG}_4}_{L^1(\Omega_H)} := \frac{\sum_{C\in C}\left\|\mathrm{v}^{\mathrm{FV}}_{h_i},(C)-\mathrm{v}^{\mathrm{dG}}_{\mathscr{P}4,h_1}(C)\right\|}{\mathrm{card}(\mathscr{C})} \quad (11)$$

$$E^{\mathrm{dG}_k}_{L^1(\Omega_H)} := \frac{\sum_{C\in C}\left\|\mathrm{v}^{\mathrm{dG}}_{\mathscr{P}k,h_1}(C)-\mathrm{v}^{\mathrm{dG}}_{\mathscr{P}4,h_1}(C)\right\|}{\mathrm{card}(\mathscr{C})} \quad (12)$$

$$E^{\mathrm{FV}_i}_{L^1(\Omega_H)} := \frac{\sum_{C\in C}\left\|\mathrm{v}^{\mathrm{FV}}_{h_i},(C)-\mathrm{v}^{\mathrm{FV}}_{h_4}(C)\right\|}{\mathrm{card}(\mathscr{C})} \quad (13)$$

where $\mathrm{v}^{\mathrm{dG}}_{\mathscr{P}k,h_1} \in \left[\mathscr{P}_k(\mathscr{T}_1)\right]^3$ and $\mathrm{v}^{\mathrm{FV}}_{h_i},(C) \in \left[\mathscr{P}_0(\mathscr{T}_i)\right]^3$ are the dG and FV velocity solutions, respectively, and $\mathrm{v}(C) \in \mathbb{R}^3$ is the velocity solution evaluated at the cell's centroid C.

The four velocity errors in 10–11-12–13 reported in Table 2 allow to cross-compare the accuracy. Asymptotic convergence towards the same numerical solution is confirmed by the monotonic decrease of $E^{\mathrm{dG}_k,\mathrm{FV}_4}_{L^1(\Omega_H)}$ and $E^{\mathrm{FV}_i,\mathrm{dG}_4}_{L^1(\Omega_H)}$. The errors associated with the $\mathrm{dG}\mathscr{P}_3(\mathscr{T}_1)$ numerical solution confirm that p-convergence is faster than h-convergence. Note in particular that

$$E^{\mathrm{dG}_3,\mathrm{FV}_4}_{L^1(\Omega_H)} < E^{\mathrm{FV}_3}_{L^1(\Omega_H)} \quad \text{and} \quad E^{\mathrm{dG}_3}_{L^1(\Omega_H)} < \frac{E^{\mathrm{FV}_3,\mathrm{dG}_4}_{L^1(\Omega_H)}}{2}.$$

Author Manuscript Author Manuscript Author Manuscript Author Manuscript

$E^{\mathrm{FV}_i}_{L^1(\Omega_H)}$ errors confirm that second order of convergence for FV numerical solution in closely approached, indeed $\log\left(\frac{E^{\mathrm{FV}_2}_{L^1(\Omega_H)}}{E^{\mathrm{FV}_3}_{L^1(\Omega_H)}}\right)/\log(2) \approx 1.85$. Accordingly, an almost four-fold decrease of the error is obtained halving the mesh step size h.

Relative velocity errors between under-resolved dG and FV computations are computed as follows

$$E^{\mathrm{dG}_k,\mathrm{FV}_i}_{L^1(\Omega_H)} := \frac{\sum_{C\in\mathscr{C}} \left\| \mathrm{v}^{\mathrm{dG}}_{\mathscr{P}k}, h_1(C) - \mathrm{v}^{\mathrm{FV}}_{h_i}(C) \right\|}{\mathrm{card}(\mathscr{C})}, \text{ with } i = k = 1, 2, \ldots, 4 \quad (14)$$

Table 3 reports velocity errors against the most accurate dG and FV solutions, see definitions 10–11, as well as under-resolved velocity errors defined in 14. It is interesting to remark that the distance between under-resolved FV and dG velocity fields $\left(E^{\mathrm{FV}_i,\mathrm{dG}_k}_{L^1(\Omega_H)}\right)$ is comparable with the distance between under-resolved FV velocity fields and the most accurate dG computations $\left(E^{\mathrm{FV}_i,\mathrm{dG}_4}_{L^1(\Omega_H)}\right)$. This suggests that, while solutions computed within the asymptotic convergence region are in good agreement, under-resolved computations differ. Accordingly FV and dG approximations approach asymptotic convergence from different paths. This observation will be confirmed by visual evaluation of velocity solutions in Section 4.3.

Figure 2 compares FVM and dGFEM based on accuracy per DOF and accuracy per JNZ. The former metric is favorable to dGFEM while the latter suggests that FVM is most efficient. Both metrics are relevant in the context of implicit formulation based on inexact Newton's method, where Newton equations are approximately solved by means of iterative solvers. Indeed the cost of a Krylov iteration scales linearly with the number of non-zeroes entries plus the number of Krylov spaces times the matrix order (equal to the number of DOFs), see *e.g.* Quarteroni *e.a.* [30].

4.3 Solution evaluation

In this Section we propose a qualitative comparison of dGFEM and FVM solutions evaluating the accuracy in *picture norm*, that is sensing the distance between increasingly accurate solutions by cross-comparing pictures depicting their most relevant features. Even if this comparison is only qualitative, the complexity of vortex structures can be guessed and the very good agreement between sufficiently resolved FV and dG solutions can be fully appreciated. Note that, for the sake of comparison, dGFEM solutions of polynomial degree k are interpolated to the nodes of the $\mathscr{T}_{i=k}$ grid.

Author Manuscript Author Manuscript Author Manuscript Author Manuscript

We first consider a velocity magnitude contour at 65cm/s, see Figures 3-4-5-6. Note that the velocity magnitude range is [0,125]cm/s for the most accurate dG and FV velocity solutions. Coarse grid FV solutions are clearly over dissipative while low polynomial degree dG solutions preserve most of the velocity solution features, being slightly under dissipative. This behavior is confirmed by the velocity magnitude range: [0,118]cm/s for the FV solution on $\mathcal{T}_1$ and [0,170]cm/s for the dG $\mathcal{P}_1(\mathcal{T}_1)$ solution. Note that the $\mathcal{P}_2(\mathcal{T}_1)$ dG solution has a number of DOFs comparable to the FV solution on $\mathcal{T}_2$ (the 1.1m mesh) whereas dG $\mathcal{P}_1(\mathcal{T}_1)$ has four times the DOFs of FV on $\mathcal{T}_1$, see Table 1.

Figure 7 focuses on hemodynimacs inside the aneurysm sac. It is possible to appreciate how $\mathcal{P}_2(\mathcal{T}_1)$ dG solutions are able to capture most of the flow features. Looking at the aneurysm alone the resemblance between second, third and fourth polynomial degree solutions is remarkable. As opposite, only the FV solution on $\mathcal{T}_3$ and $\mathcal{T}_4$ are able to satisfactorily reproduce the intensity of the primary vortex inside the aneurysm balloon, note in particular the peak velocity “gust” travelling near the aneurysm wall.

5 Discussion and Conclusions

The outcome of this work can be considered trivial: given the same computational domain and numerically solving the same equations with the same steady state boundary flow conditions over it, convergence towards the same numerical solution is observed. This is the expected result, even employing different spatial discretizations. Nevertheless, how fine the grid should be and how high the polynomial degree should be to approach mesh independence is a crucial point that need to be addressed, at least from the viewpoint of the relevance of the question itself, see also Valen-Sendstad *e.a.* [35]. We demonstrated that meshes that are considered fine-enough to accurately capture hemodynamics might lead to under-resolved velocity fields. Moreover, we show that, even if solutions computed within the asymptotic convergence region are similar, different approximation schemes can approach asymptotic convergence from different paths. Underestimating the issue can lead to frustration when validating against experiments. For example, overly diffusive FV velocity fields could be in better agreement than FE velocity fields if compared with under-resolved Particle Image Velocimetry (PIV) acquisitions.

The accuracy versus DOFs and JNZs analysis reported in Section 4 shows the benefits of high-order polynomial expansions from the convergence rate viewpoint. In this regard, the ability of mesh generators to provide satisfactory approximations of domain boundaries with a number of mesh elements that suits the solver requirements is of crucial importance. Indeed, since increasing the polynomial degree provides more accuracy per DOF, coarser meshes would allow to further raise the polynomial degree without incurring in excessive computational costs (due to an excessive growth of the number of DOFs and JNZs). Unfortunately, given the complexity of the vascular district geometries, the generation of coarse meshes providing satisfactory approximations of domain boundaries is a user dependent and time consuming practice. Further research efforts in the field of high-order

Author Manuscript Author Manuscript Author Manuscript Author Manuscript

mesh generation techniques are required to streamline and automate the meshing stage, see *e.g.* [3]-[7].

Since spatial accuracy is a prerequisite for considering high-order accurate unsteady flow computations, the present investigation can be considered a preliminary step to tackle physiologic pulsatile flow conditions. Indeed, the mesh density and polynomial degree requirements identified by means of steady flow simulations can be safely extrapolated to unsteady flow computations provided that the peak Reynolds number (observed at the systolic peak) is simulated. Roughly speaking, since the higher the Reynolds number the higher the spatial accuracy requirements, the worst case scenario should be taken into account. As a limitation to the proposed approach, it is worth to mention that steady state boundary flow conditions might lead to the onset of flow instabilities if the flow is convection dominated. This can be observed at moderate Reynolds numbers, lower than those associated with transition to turbulence, see *e.g.* [15]. In this occurrence numerical studies combining high-order accurate time integration with high-order accurate spatial discretizations should be performed.

This paper demonstrates the urge for *a posteriori* error estimation strategies, possibly in combination with adaptive numerical methods that could reduce the error by local enrichments at a minimal computational expense. Even if such strategies exist, their actual application in the field of computational hemodynamics seems to be quite limited. As an extenuating circumstance, it should be considered that several sources of uncertainty might dominate over the spatial and temporal errors of the numerical solution. Consider the following incomplete list. i) The uncertainty in the computational domain representation. ii) The uncertainty in boundary conditions imposed on fictitious inflow and outflow boundaries, see *e.g.* Heywood *e.a.* [22]. iii) The assumption of rigid walls or the uncertainty in actual response of the wall in fluid-structure interaction computations. iv) The uncertainty in the constitutive law for blood, in particular for low-speed flows or high-speed flows with transition to turbulence. In order to give precise meaning to accuracy requirements, precision should be related to uncertainty in the inputs to the mathematical model by means of sensitivity analysis. The present investigation does not address this important aspect but demonstrates that accurate enough computations (with fine enough meshes and/or high-enough polynomial degrees in case of FV and dGFEM computations, respectively) will be required to do so.

Acknowledgements

We acknowledge the CINECA HPC facility for the availability of high performance computing resources and support within the agreement “Convenzione di Ateneo Università degli Studi di Bergamo”. HM acknowledges support from the National Institutes of Health (Grant no. R01 NS091075 and R03 NS090193) and Toshiba Medical System Corporation.

References

[1]. Antiga L, Piccinelli M, Botti L, Ene-Iordache B, Remuzzi A, and Steinman DA. An image-based modeling framework for patient-specific computational hemodynamics. Medical & Biological Engineering & Computing, 46(11):1097–1112, 2008. [PubMed: 19002516]

Author Manuscript Author Manuscript Author Manuscript Author Manuscript

[2]. Babuška I and Suri M. The p and h-p versions of the finite element method, basic principles and properties. SIAM Review, 36(4):578–632, 1994.

[3]. Bassi F, Botti L, and Colombo A. Agglomeration based physical frame dG discretizations: An attempt to be mesh free. Mathematical Models and Methods in Applied Sciences, 24(08):1495–1539, 2014.

[4]. Bassi F, Crivellini A, Di Pietro DA, and Rebay S. An artificial compressibility flux for the discontinuous Galerkin solution of the incompressible Navier-Stokes equations. J. Comput. Phys, 218:794–815, 2006.

[5]. Bassi F, Massa F, Botti L, and Colombo A. Artificial compressibility Godunov fluxes for variable density incompressible flows. Computers & Fluids, 2017 Published online.

[6]. Bassi F, Rebay S, Mariotti G, Pedinotti S, and Savini M. A high-order accurate discontinuous finite element method for inviscid and viscous turbomachinery flows. In Decuypere R and Dibelius G, editors, Proceedings of the 2nd European Conference on Turbomachinery Fluid Dynamics and Thermodynamics, pages 99–108, Antwerpen, Belgium, 1997 Technologisch Instituut.

[7]. Bazilevs Y, Calo VM, Zhang Y, and Hughes TJR. Isogeometric fluid–structure interaction analysis with applications to arterial blood flow. Computational Mechanics, 38(4):310–322, 2006.

[8]. Benzi M, Golub GH, and Liesen J. Numerical solution of saddle point problems. ACTA NUMERICA, 14:1–137, 2005.

[9]. Berg P, Roloff C, Beuing O, Voss S, Sugiyama S-I, Aristokleous N, Anayiotos AS, Ashton N, Revell A, Bressloff NW, Brown AG,Jae Chung B, Cebral JR, Copelli G, Fu W, Qiao A, Geers AJ, Hodis S, Dragomir-Daescu D, Nordahl E, Bora Suzen Y, Owais Khan M, Valen-Sendstad K, Kono K, Menon PG, Albal PG, Mierka O, Münster R, Morales HG, Bonnefous O, Osman J, Goubergrits L, Pallares J, Cito S, Passalacqua A, Piskin S, Pekkan K, Ramalho S, Marques N, Sanchi S, Schumacher KR, Sturgeon J, Švihlová H, Hron J, Usera G, Mendina M, Xiang J, Meng H, Steinman DA, and Janiga G. The computational fluid dynamics rupture challenge 2013—phase ii: Variability of hemodynamic simulations in two intracranial aneurysms. Journal of Biomechanical Engineering, 137(12):121008–121008–13, 11 2015.

[10]. Bertagna L, Deparis S, Formaggia L, Forti D, and Veneziani A. The LifeV library: engineering mathematics beyond the proof of concept. ArXiv e-prints, 2017.

[11]. Botti L. A choice of forcing terms in inexact Newton iterations with application to pseudo-transient continuation for incompressible fluid flow computations. Applied Mathematics and Computation, 266:713 – 737, 2015.

[12]. Botti L, Colombo A, and Bassi F. h-multigrid agglomeration based solution strategies for discontinuous galerkin discretizations of incompressible flow problems. Journal of Computational Physics, 347(Supplement C):382 – 415, 2017.

[13]. Botti L and Di Pietro DA. A pressure-correction scheme for convection dominated incompressible flows with discontinuous velocity and continuous pressure. Journal of Computational Physics, 230(3):572–585, 2011.

[14]. Botti L, Piccinelli M, Ene-Iordache B, Remuzzi A, and Antiga L. An adaptive mesh refinement solver for large-scale simulation of biological flows. International Journal for Numerical Methods in Biomedical Engineering, 26(1):86–100, 2010.

[15]. Botti L, Van Canneyt K, Kaminsky R, Claessens T, Planken RN, Verdonck P, Remuzzi A, and Antiga L. Numerical evaluation and experimental validation of pressure drops across a patient-specific model of vascular access for hemodialysis. Cardiovascular Engineering and Technology, 4(4):485–499, 12 2013.

[16]. Boussel L, Rayz V, McCulloch C, Martin A, Acevedo-Bolton G, Lawton M, Higashida R, Smith WS, Young WL, and Saloner D. Aneurysm growth occurs at region of low wall shear stress: Patient-specific correlation of hemodynamics and growth in a longitudinal study. Stroke; a journal of cerebral circulation, 39(11):2997–3002, 11 2008.

[17]. Cebral J, Mut F, Weir J, and Putman C. Quantitative characterization of the hemodynamic environment in ruptured and unruptured brain aneurysms. American Journal of Neuroradiology, 32(1):145–151, 2011. [PubMed: 21127144]

Author Manuscript Author Manuscript Author Manuscript Author Manuscript

[18]. Cebral JR, Castro MA, Burgess JE, Pergolizzi RS, Sheridan MJ, and Putman CM. Characterization of cerebral aneurysms for assessing risk of rupture by using patient-specific computational hemodynamics models. American Journal of Neuroradiology, 26(10):2550–2559, 2005. [PubMed: 16286400]

[19]. Chorin AJ. A numerical method for solving incompressible viscous flow problems. Journal of Computational Physics, 135(2):118 – 125, 1997.

[20]. Elsworth D and Toro E. Riemann solvers for solving the incompressible Navier-Stokes equations using the artificial compressibility method. Technical Report 9208, College of Aeronautics, Cranfield Institute of Technology, 1992.

[21]. Geuzaine C and Remacle J-F. Gmsh: A 3-d finite element mesh generator with built-in pre- and post-processing facilities. International Journal for Numerical Methods in Engineering, 79(11): 1309–1331, 2009.

[22]. Heywood JG, Rannacher R, and Turek S. Artificial boundaries and flux and pressure conditions for the incompressible Navier-Stokes equations. International Journal for Numerical Methods in Fluids, 22(5):325–352, 1996.

[23]. Janiga G, Berg P, Sugiyama S, Kono K, and Steinman D. The computational fluid dynamics rupture challenge 2013—phase i: Prediction of rupture status in intracranial aneurysms. American Journal of Neuroradiology, 36(3):530–536, 2015. [PubMed: 25500315]

[24]. Kelley C and Keyes D. Convergence analysis of pseudo-transient continuation. SIAM Journal on Numerical Analysis, 35(2):508–523, 1998.

[25]. Klein B, Kummer F, and Oberlack M. A simple based discontinuous galerkin solver for steady incompressible flows. Journal of Computational Physics, 237(Supplement C):235 – 250, 2013.

[26]. Meng H, Tutino V, Xiang J, and Siddiqui A. High wss or low wss? complex interactions of hemodynamics with intracranial aneurysm initiation, growth, and rupture: Toward a unifying hypothesis. American Journal of Neuroradiology, 35(7):1254–1262, 2014. [PubMed: 23598838]

[27]. Metaxa E, Tremmel M, Natarajan SK, Xiang J, Paluch RA, Mandelbaum M, Siddiqui AH, Kolega J, Mocco J, and Meng H. Characterization of critical hemodynamics contributing to aneurysmal remodeling at the basilar terminus in a rabbit model. Stroke, 41(8):1774–1782, 2010. [PubMed: 20595660]

[28]. Mulder WA and Van Leer B. Experiments with implicit upwind methods for the Euler equations. Journal of Computational Physics, 59(2):232–246, 1985.

[29]. Paliwal N, Damiano RJ, Varble NA, Tutino VM, Dou Z, Siddiqui AH, and Meng H. Methodology for computational fluid dynamic validation for medical use: Application to intracranial aneurysm. Journal of Biomechanical Engineering, 139(12):121004–121004–10, 9 2017.

[30]. Quarteroni A, Sacco R, and Saleri F. Numerical Mathematics, volume 37 Springer Verlag, Berlin, 2000.

[31]. Shahbazi K, Fischer PF, and Ethier CR. A high-order Discontinuous Galerkin method for the unsteady incompressible Navier-Stokes equations. J. Comput. Phys, 222(1):391–407, 2007.

[32]. Témam R. Sur l'approximation de la solution des équations de Navier-Stokes par la méthode des pas fractionnaires (II). Archive for Rational Mechanics and Analysis, 33:377–385, 1969.

[33]. Toulorge T, Geuzaine C, Remacle J-F, and Lambrechts J. Robust untangling of curvilinear meshes. Journal of Computational Physics, 254:8 – 26, 2013.

[34]. Updegrove A, Wilson NM, Merkow J, Lan H, Marsden AL, and Shadden SC. Simvascular: An open source pipeline for cardiovascular simulation. Annals of Biomedical Engineering, 45(3): 525–541, 2017. [PubMed: 27933407]

[35]. Valen-Sendstad K, Piccinelli M, and Steinman DA. High-resolution computational fluid dynamics detects flow instabilities in the carotid siphon: Implications for aneurysm initiation and rupture? Journal of Biomechanics, 47(12):3210–3216, 2014. [PubMed: 25062933]

[36]. Xiang J, Natarajan SK, Tremmel M, Ma D, Mocco J, Hopkins LN, Siddiqui AH, Levy EI, and Meng H. Hemodynamic–morphologic discriminants for intracranial aneurysm rupture. Stroke, 42(1):144–152, 2010. [PubMed: 21106956]

Author Manuscript Author Manuscript Author Manuscript Author Manuscript

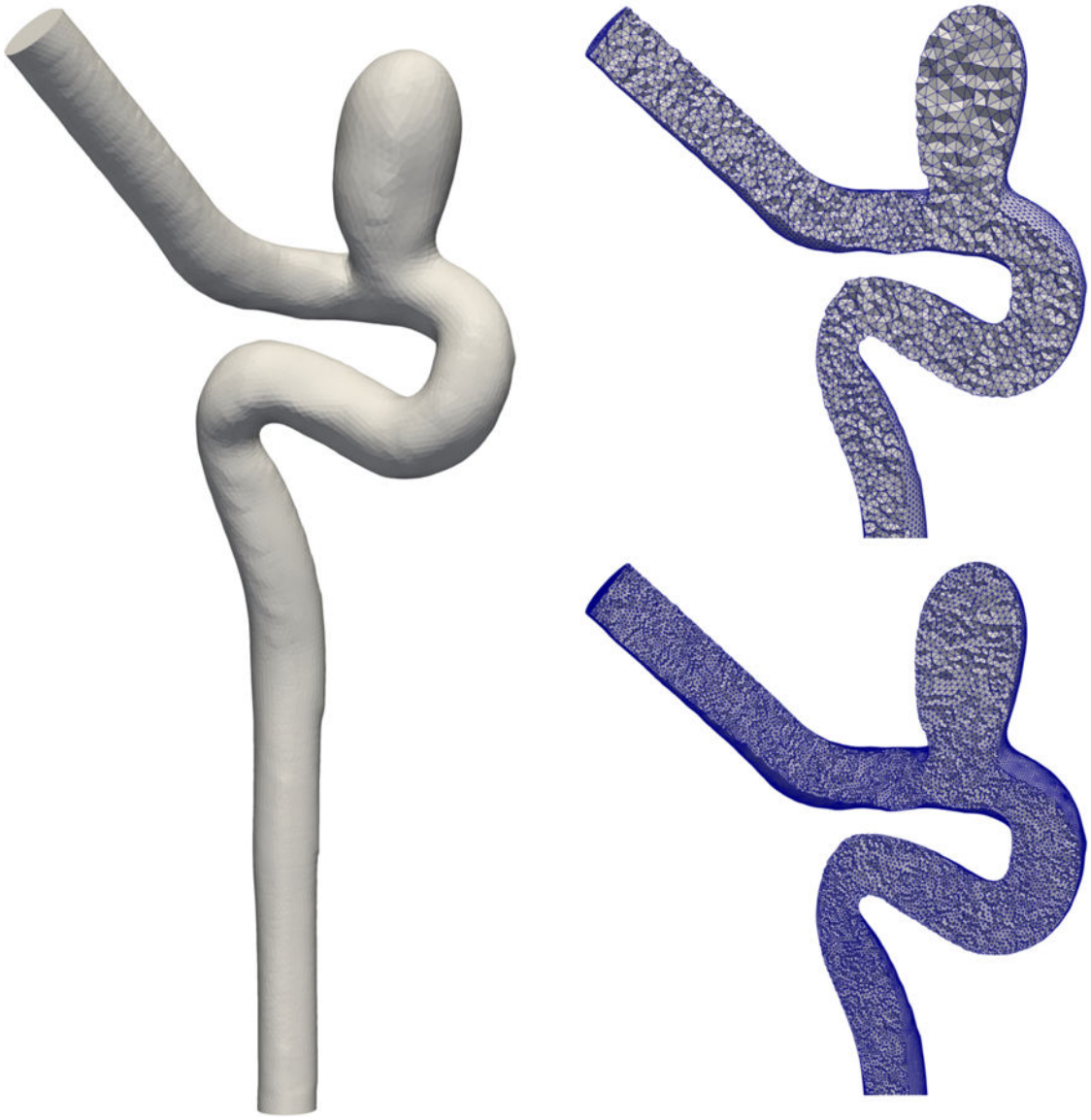

Figure 1:

Approximated IA vascular district geometry Ω_H. *Left*, surface mesh of $\partial\Omega_H$. *Right*, clip of $\{\mathcal{T}_1\}$ and $\{\mathcal{T}_2\}$ (*top* and *bottom*, 134k and 1.07m elements, respectively) showing tetrahedral elements within the fluid domain.

Author Manuscript Author Manuscript Author Manuscript Author Manuscript

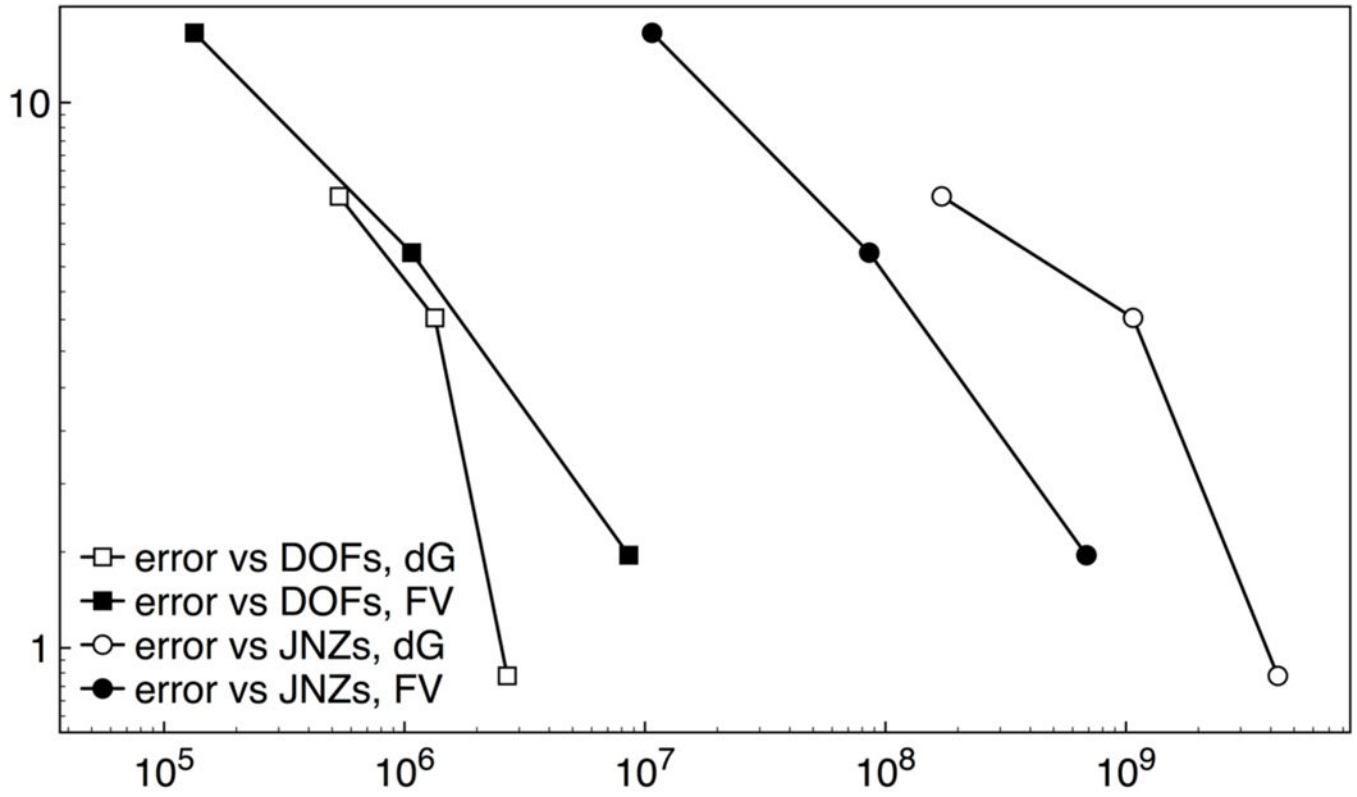

Figure 2:

Comparison of the velocity error in $L^1(\Omega_H)$ norm against DOFs (square dots) and JNZs (circular dots) for FV (filled dots) and dG (empty dots) discretizations. Increasingly accurate FV and dG solutions are obtained by means of *h*-refinement and *p*-refinement, respectively. Velocity errors for FV and dG dicretizations are computed as defined in 13 and 12, respectively.

Author Manuscript Author Manuscript Author Manuscript Author Manuscript

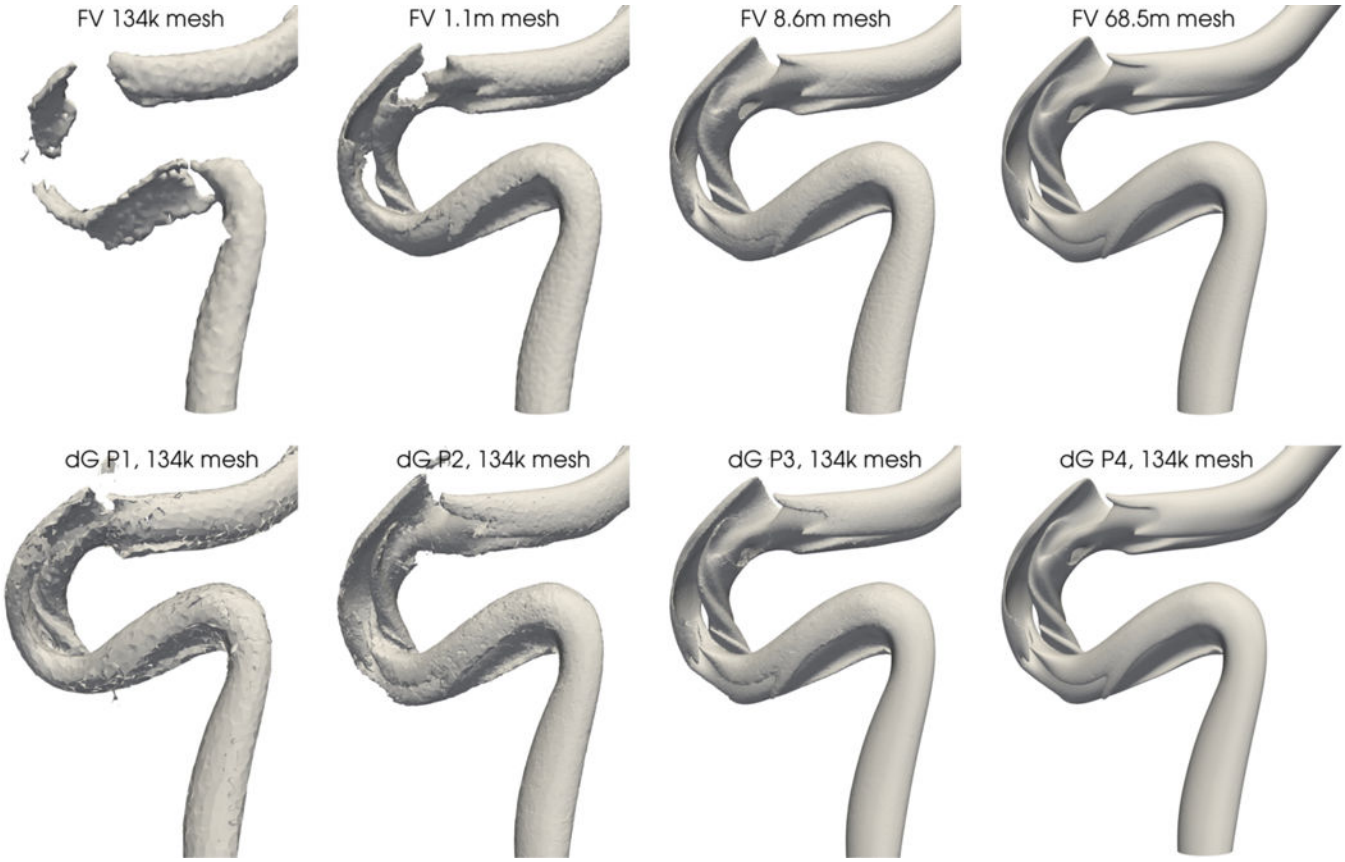

Figure 3:

Velocity magnitude contour at 65cm/s (*front view*). Qualitative comparison of FVM (first row, $\mathcal{T}_{1,2,3,4}$ meshes) and dGFEM (second row, $\mathcal{P}_{1,2,3,4}$ polynomial spaces) increasingly accurate solutions (from left to right).

Author Manuscript Author Manuscript Author Manuscript Author Manuscript

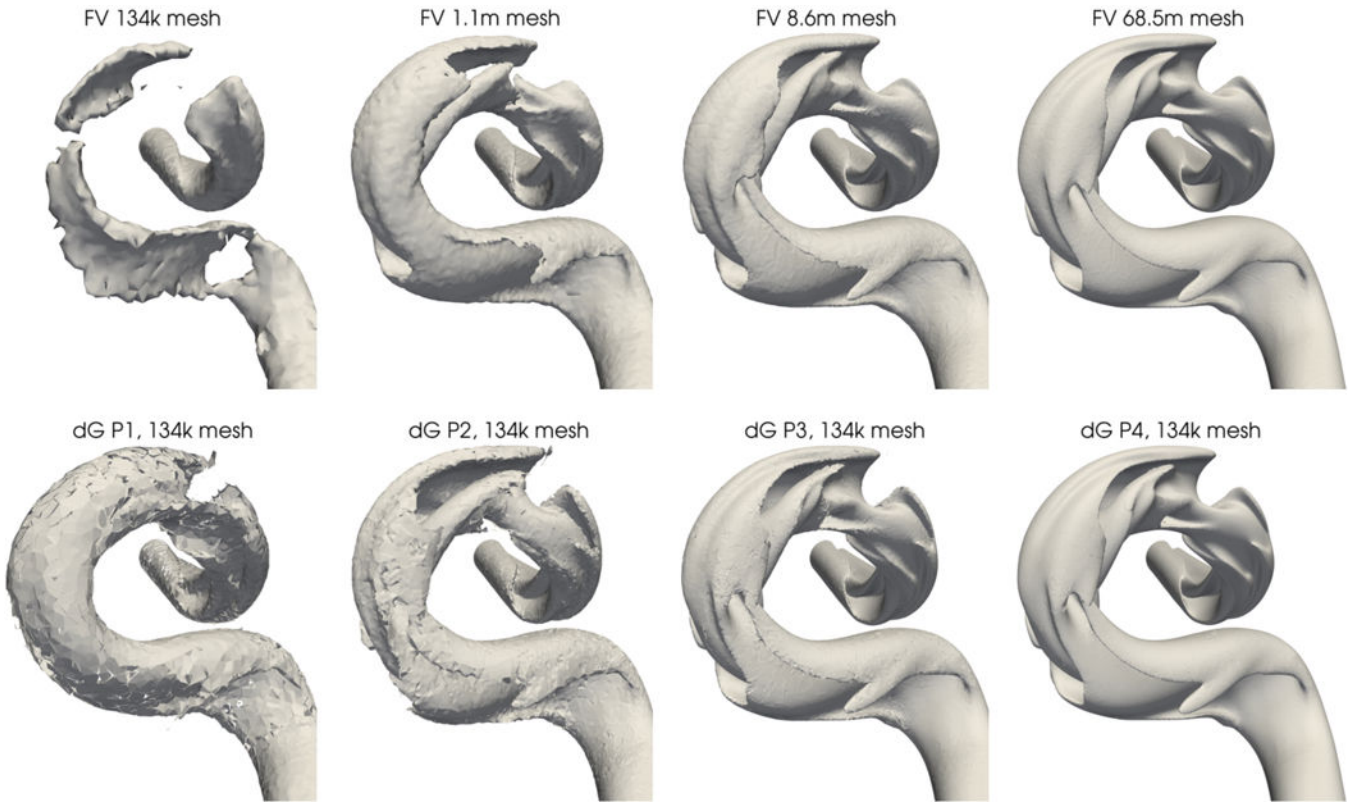

Figure 4:

Velocity magnitude contour at 65cm/s (*rear view*). Qualitative comparison of FVM (first row, $\mathcal{T}_{1,2,3,4}$ meshes) and dGFEM (second row, $\mathcal{P}_{1,2,3,4}$ polynomial spaces) increasingly accurate solutions (from left to right).

Author Manuscript Author Manuscript Author Manuscript Author Manuscript

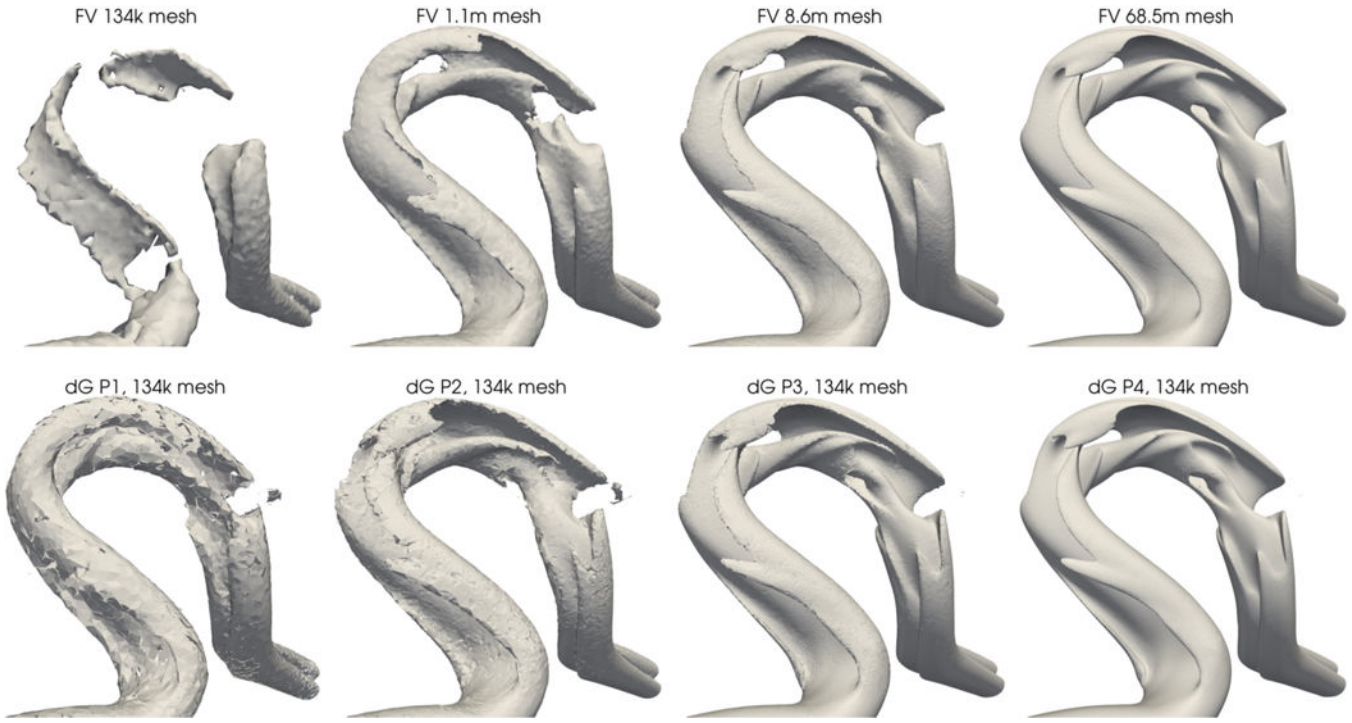

Figure 5:

Velocity magnitude contour at 65cm/s (*back view*). Qualitative comparison of FVM (first row, $\mathcal{T}_{1,2,3,4}$ meshes) and dGFEM (second row, $\mathcal{P}_{1,2,3,4}$ polynomial spaces) increasingly accurate solutions (from left to right).

Author Manuscript Author Manuscript Author Manuscript Author Manuscript

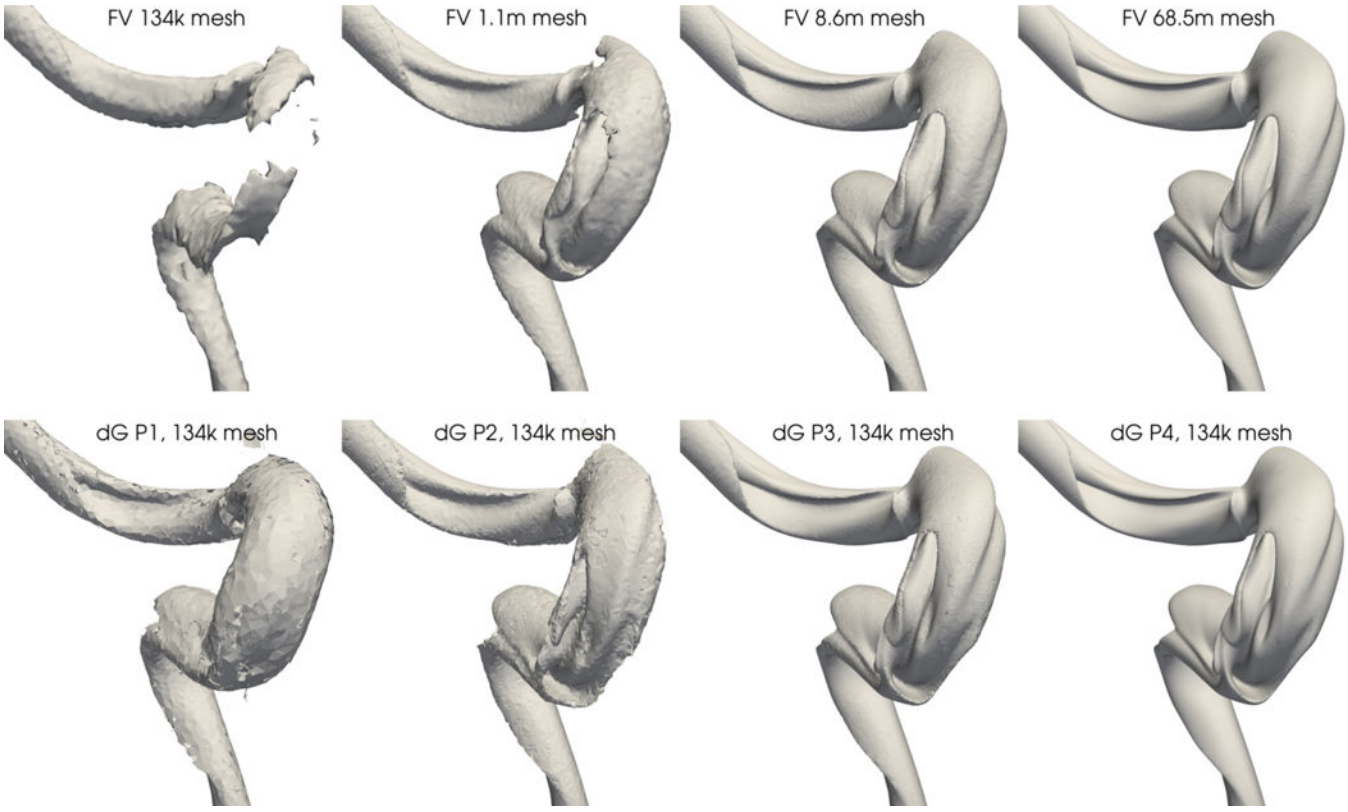

Figure 6:

Velocity magnitude contour at 65cm/s (*back view*). Qualitative comparison of FVM (first row, $\mathcal{T}_{1,2,3,4}$ meshes) and dGFEM (second row, $\mathcal{P}_{1,2,3,4}$ polynomial spaces) increasingly accurate solutions (from left to right).

Author Manuscript Author Manuscript Author Manuscript Author Manuscript

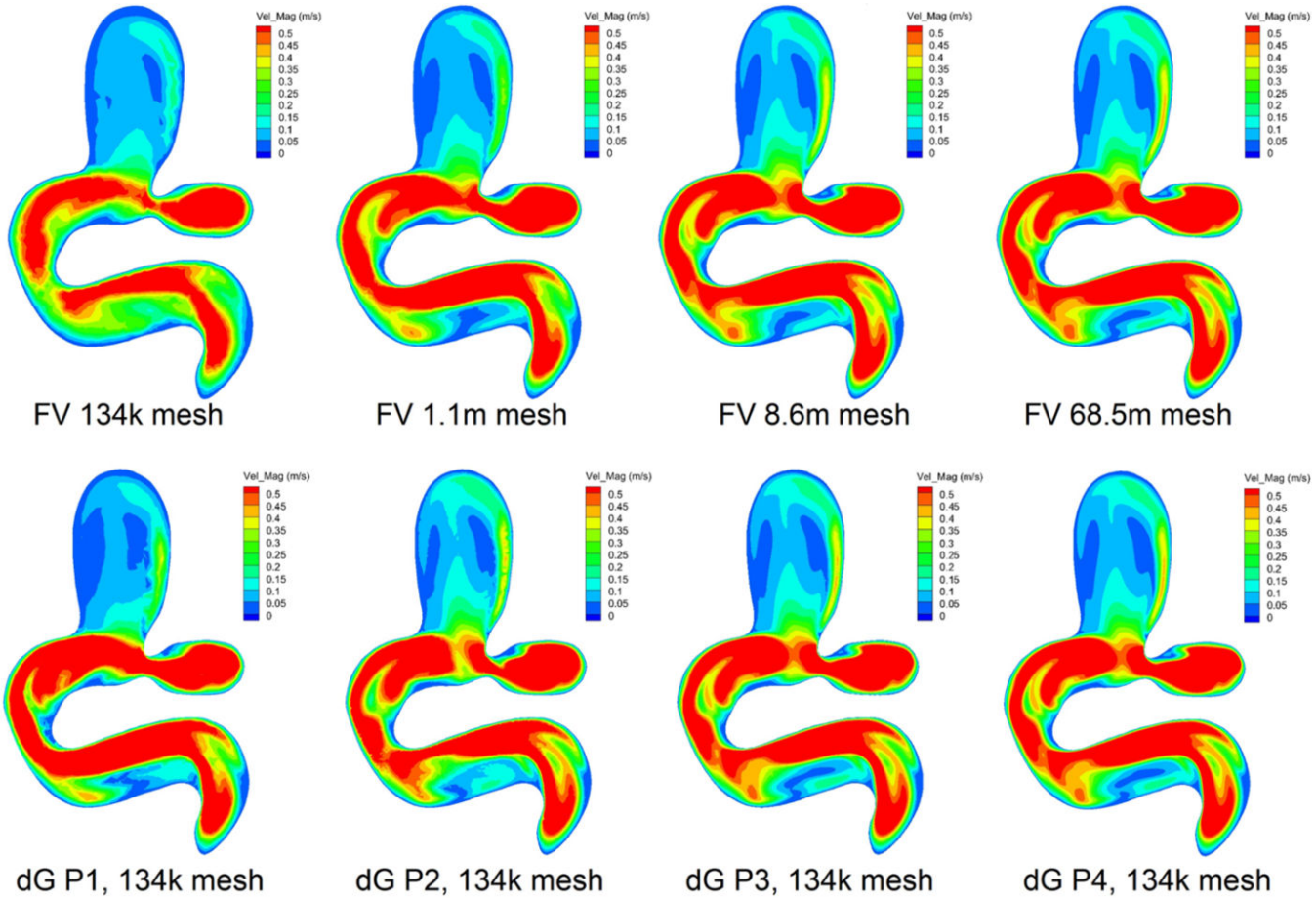

Figure 7:

Velocity magnitude on a plane cutting the aneurysm in two halves. Qualitative comparison of FVM (first row, $\mathcal{T}_{1,2,3,4}$ meshes) and dGFEM (second row, $\mathcal{P}_{1,2,3,4}$ polynomial spaces) increasingly accurate solutions. All sub-figures use the same 12-colors RGB map for the interval $[50-0] cm/s$.

Author Manuscript

Author Manuscript

Author Manuscript

Author Manuscript

Table 1:

Number of Degrees Of Freedom (DOFs) and Jacobian Non-Zeroes (JNZs) of dG and FV discretizations.

		dG			FV	
polynomial space	**grid**	**DOFs**	**JNZs**	**grid**	**DOFs**	**JNZs**
$\mathscr{P}_1$	$\mathscr{T}_1$	535k	171.2m	$\mathscr{T}_1$	134k	10.7m
$\mathscr{P}_2$	$\mathscr{T}_1$	1.34m	1.070b	$\mathscr{T}_2$	1.07m	85.62m
$\mathscr{P}_3$	$\mathscr{T}_1$	2.67m	4.280b	$\mathscr{T}_3$	8.56m	684.9m
$\mathscr{P}_4$	$\mathscr{T}_1$	4.68m	13.11b	$\mathscr{T}_4$	68.5m	5.48b

Author Manuscript Author Manuscript Author Manuscript Author Manuscript

Table 2:

Cross-comparison of velocity error in $L^1(\Omega_H)$ norm. $E^{\mathrm{dG}_k}_{L^1(\Omega_H)}$ and $E^{\mathrm{FV}_i}_{L^1(\Omega_H)}$ compare the error of dGFEM and FVM against the most accurate dG and FV solution, respectively. $E^{\mathrm{dG}_k,\mathrm{FV}_4}_{L^1(\Omega_H)}$ and $E^{\mathrm{FV}_i,\mathrm{dG}_4}_{L^1(\Omega_H)}$ compare the error of dGFEM and FVM against the most accurate FV and dG solution, respectively, see text for details.

	dG error [cm/s]			FV error [cm/s]	
polynomial degree	$E^{\mathrm{dG}_k}_{L^1(\Omega_H)}$	$E^{\mathrm{dG}_k,\mathrm{FV}_4}_{L^1(\Omega_H)}$	**mesh index**	$E^{\mathrm{FV}_i,\mathrm{dG}_4}_{L^1(\Omega_H)}$	$E^{\mathrm{FV}_i}_{L^1(\Omega_H)}$
$k = 1$	6.73003	6.54353	$i = 1$	13.4277	13.4227
$k = 2$	4.02893	4.12215	$i = 2$	5.58825	5.30604
$k = 3$	0.88863	1.29241	$i = 3$	2.07106	1.47922
$k = 4$	-	0.83734	$i = 4$	0.83734	-
ref. sol.	$\mathrm{dG}\mathscr{P}_4(\mathscr{T}_1)$	$\mathrm{FV}\mathscr{T}_4$	ref. sol.	$\mathrm{dG}\mathscr{P}_4(\mathscr{T}_1)$	$\mathrm{FV}\mathscr{T}_4$

Author Manuscript

Author Manuscript

Author Manuscript

Author Manuscript

Table 3:

Cross-comparison of velocity error in $L^1(\Omega_H)$ norm. $E^{\mathrm{dG}_k,\mathrm{FV}_4}_{L^1(\Omega_H)}$ and $E^{\mathrm{FV}_i,\mathrm{dG}_4}_{L^1(\Omega_H)}$ compare the error of dGFEM and FVM against the most accurate FV and dG solution, respectively. $E^{\mathrm{FV}_i,\mathrm{dG}_k}_{L^1(\Omega_H)}$ compares the error of under-resolved FV and dG computations.

dG vs. FV	$E^{\mathrm{FV}_i,\mathrm{dG}_k}_{L^1(\Omega_H)}$	$E^{\mathrm{dG}_k,\mathrm{FV}_4}_{L^1(\Omega_H)}$	$E^{\mathrm{FV}_i,\mathrm{dG}_4}_{L^1(\Omega_H)}$
$i = k = 1$	11.7134	6.54353	13.4277
$i = k = 2$	5.31248	4.12215	5.58825
$i = k = 3$	2.18439	1.29241	2.07106
$i = k = 4$	0.83734	0.83734	0.83734